Check for updates

applied optics

Unimorph mirror for adaptive optics in space telescopes

DAVID ALALUF,[1,2,*] RENAUD BASTAITS,[1] KAINAN WANG,[1] MIHAITA HORODINCA,[3] GRÉGORY MARTIC,[4] BILAL MOKRANI,[5] AND ANDRÉ PREUMONT[1]

[1]Université Libre de Bruxelles, Department of Control Engineering and System Analysis, Active Structures Laboratory, Belgium
[2]European Space Agency—ESA/ESTEC, Opto-Electronics section, Noordwijk, The Netherlands
[3]Technical University "Gheorghe Asachi", Department of Machine-Tools and Tools, Iasi, Romania
[4]Belgian Ceramic Research Centre, Mons, Belgium
[5]Department of Mechanical, Materials and Aerospace Engineering, University of Liverpool, The Quadrangle, Brownlow Hill L69 3GH, UK
*Corresponding author: David.Alaluf@esa.int

Received 9 January 2018; revised 12 March 2018; accepted 1 April 2018; posted 3 April 2018 (Doc. ID 319196); published 2 May 2018

This paper presents a unimorph deformable mirror intended to be used as secondary corrector in space telescopes. The deformable mirror consists of a single-crystal silicon wafer (76.2 mm diameter, 500 μm thickness) covered with an optical coating on the front side and an array of 25 independent piezoelectric transducer (PZT) actuators acting in d_{31} mode on the back side. The mirror is mounted on an isostatic support with three position linear actuators controlling the rigid-body motion. The first part of the paper presents the experimental results obtained with the manufactured prototype. The mirror was tested in terms of root mean square (RMS) wavefront error, open-loop long-term stability, voltage budget for active control, rigid-body actuation, reflectivity, and dynamic response. The prototype is fully compliant with the requirements set by the European Space Agency (ESA). The second part of the paper, purely based on numerical simulations, presents a robust way to face thermal distortion, inherent to unimorph architecture. © 2018 Optical Society of America

OCIS codes: (010.1080) Active or adaptive optics; (230.4040) Mirrors; (350.6090) Space optics; (120.6085) Space instrumentation; (110.6770) Telescopes; (120.6810) Thermal effects.

https://doi.org/10.1364/AO.57.003629

1. INTRODUCTION

Adaptive optics (AO) has been successfully used to improve the image quality provided by terrestrial telescopes. AO systems use a deformable mirror (DM), located in the optical train of the telescope, deformed mechanically with a set of actuators to produce a wavefront correction opposing both the wavefront error induced by the atmospheric turbulence, as well as the residual error of the active optics [1,2]. The main parameters of a DM are the number of actuators (number of independent degrees of freedom), the stroke (typically a few microns), the size [from microsystems up to several meters for the future European Extremely Large Telescope (E-ELT); the size of the DM is related to the field of view], and the temporal bandwidth (typically 50–100 Hz, which brings a lower limit to the first natural frequency of the mirror). The linearity and hysteresis have only a second-order impact on performance in the closed-loop. More recently, the space telescope community has been interested in using DMs to compensate for manufacturing errors, gravity release, and thermal distortion affecting large lightweight mirrors in space telescopes ($D > 0.5$ m) [3–5]. The main challenges in the design of a DM for space telescopes lie in meeting conflicting constraints. Indeed, the mirror has to be thin and soft to allow large strokes, while warranting a very high optical surface quality and a reasonable first resonance frequency. Furthermore, high amplitude deformations require high voltages, as well as large gaps between the actuators, whereas, the wider the gap, the worse the surface accuracy. Besides, the supporting mount of the mirror has to be soft to allow free expansion of the mirror, but strong enough to withstand the accelerations during the launch of the spacecraft. Last, but not least, the DM has to fulfill all of those requirements in a harsh space environment (with high temperature variations, inducing thermal distortion of the mirror, cosmic radiations, etc.). Thanks to its simple architecture, the unimorph technology can offer high reliability; hence, it is a good candidate for space applications. A unimorph DM, intended to be used in space telescopes, has been presented by Rausch in Ref. [6]. It consists of a 550-μm-thick glass substrate bonded to a 700-μm-thick piezoelectric disc (using voltages between −400 V and +400 V). The mirror uses 41 electrodes for the shape control and three external active rings for the tip/tilt correction. Although the mirror presents interesting optical and

controllability features, it turned out that the mirror was not strong enough to survive the full vibrations test campaign due to the failure of the fragile external arms [7]. Besides that, the thermal balancing of the mirror is achieved by selecting materials with a close coefficient of thermal expansion (CTE), which restricts the materials choice. Furthermore, it uses high symmetric positive and negative voltages, which is not recommended (to prevent from damaging the piezoelectric material [8]).

The first part of this paper presents the experimental performance of a unimorph DM developed on behalf of the European Space Agency (ESA), in the framework of the GSTP program BIALOM [9]. The DM is capable of generating the first 15 Zernike modes (with positive voltages only) with a root mean square (RMS) error smaller than 30 nm. The mirror is supported by an active isostatic support, designed to have a negligible impact on the shaping of the mirror, allowing control of the tip/tilt modes. The DM uses only space qualified components and has to meet the requirements summarized in Tables 1 and 2. These requirements have been established by ESA, based on existing Korsch-type telescopes (e.g., Pléiades), as well as on the expertise of our partner AMOS in the design and manufacturing of large lightweight aluminum primary mirrors (>700 mm diameter with a honeycomb-type back face, a remaining surface skin thickness of 3 mm, and an areal density of 25 kg/m^2). The compensation of the low-order Zernike modes (Z_4–Z_{11}) is of utmost importance. In particular, the dominant term is astigmatism [reaching up to 2 μm peak-to-valley (PV) in the worst case], where the other terms are lower than 1 μm PV and lower than 0.5 μm PV for the optional Z_{12} to Z_{15}. In contrast to terrestrial telescopes, whose goal is to counteract fast wavefront distortions induced by atmospheric turbulence, the goal of the present application is to maintain the creep as small as possible over a timescale of hours to compensate for static or slow disturbances (such as thermal distortion).

The second part of the paper, purely based on numerical simulations, presents another design, based on a PZT ring bonded on the optical face of the mirror, whose goal is twofold: (i) to cope with thermal distortion of the mirror due to CTE mismatch between its materials and (ii) to control the mirror in both directions with only positive voltages. Other designs using a PZT ring have been presented in Refs. [10,11]. Contrary to the design proposed in the present paper, these mirrors are used in a clamped configuration, and the PZT ring is bonded on the back face of the mirror. The clamped configuration guarantees a very high first resonance frequency, but largely impacts the stroke, as well as the RMS error on the Zernike modes.

The paper is organized as follows: section 2.A presents the design and the manufacturing process of the DM. Section 2.B describes the finite element (F.E.) model. Section 2.C introduces the control strategy and compares two methods singular value decomposition (SVD) and damped least squares (DLS) to deal with the ill-conditioning of the Jacobian. Section 2.D reports on experimental results and presents a new ultra-flat design. Section 3.A analytically and numerically demonstrates that a passive ring can be used to thermally balance the mirror. Finally, section 3.B shows how a PZT ring can be combined with the central PZT patch to drive the mirror with only positive voltages and to obtain a thermally balanced design.

Table 1. General Compliance Matrix

	Requirement
RMS error (for Z_1–Z_{15})	$\lambda/20$ at 633 nm
Long-term stability (in open-loop)	1 h
Voltage range for active control	<50% of V_{max}
Reflectivity at 633 nm	>95%
Optical surface roughness	<2 nm
Lowest eigen frequency	140 Hz
Design load	20 g

Table 2. Amplitude Requirements of the Zernike Modes in an Optical Pupil of 30 mm Diameter[a]

Zernike Mode		PV [nm]
Z4	Defocus	1000
Z5	Oblique astigmatism	2000
Z6	Vertical astigmatism	2000
Z7	Vertical coma	1000
Z8	Horizontal coma	1000
Z9	Vertical trefoil	500
Z10	Oblique trefoil	500
Z11	Spherical aberration	750
Z12	Secondary astigmatism vertical	500
Z13	Secondary astigmatism oblique	500
Z14	Vertical Tetrafoil	500
Z15	Oblique Tetrafoil	500

[a] Z12–Z15 are optional modes.

2. PART 1

A. Design and Manufacturing of the Mirror

The mirror consists of a single-crystal Si wafer (76.2 mm diameter, 500 μm thickness) covered with a high-quality Al optical coating on the front side, so as to reach a reflectivity higher than 97% for wavelengths around 633 nm. The rear face of the wafer is covered with an Al ground electrode, on which is glued a thin PZT patch (50 mm diameter, 200 μm thickness), operating in the d_{31} mode [12–14]. The commercial PZT patch (PIC-252 from PI Ceramic) is supplied with a single thin metallic Cu/Ni electrode of ≈1 μm thickness. Before the gluing of the PZT patch on the Si mirror, the desired electrode pattern is obtained by laser ablation of the continuous Cu/Ni electrode (with a gap of 200 μm to avoid arcing within the PZT). For the present application, it is shown that with only 25 actuators the DM is fully compliant with all the requirements. This constitutes by no means a limitation, for the number of actuators may be increased if needed; note, however, that the fill factor (ratio between the useful area covered by the electrodes and the full area within the optical pupil) will reduce as the number of electrodes increases. As shown in Fig. 1, the electrodes are arranged in a keystone pattern, modified to include tracks and outer pads in order to bring all of the electrical connections at the periphery of the PZT. This allows rejection of potential defects induced by the wires (local print-through and depolarizing of the PZT material during the soldering process) outside the optical pupil. F.E. simulations showed that the tracks do not jeopardize

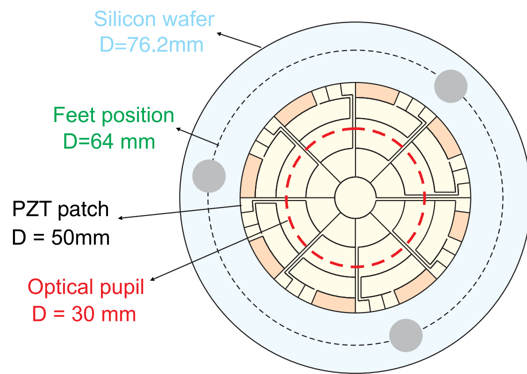

Fig. 1. Geometry of the deformable mirror (isostatic support, keystone electrode design, electric tracks, and optical pupil).

the ability to meet the specifications, particularly with thin tracks (200 μm width). Indeed, thanks to the laser ablation, the fill factor is 94%, which is very high compared to any other DM technology, limiting the print-through error (caused by the gaps and the tracks) to a value smaller than 1.5 nm RMS for a 1 μm amplitude defocus.

The DM is connected to a lightweight support plate through an active isostatic mount. The main challenges in the design of the isostatic support lie in meeting the conflicting requirements: (i) The support must allow thermal differential expansion between the mirror and its supporting structure and (ii) if the system is to be used as a wavefront corrector in a space telescope, the mirror assembly must withstand the strong accelerations associated with the space qualification, which requires a strong connection between the mirror and its support, and a large enough natural frequency. The adopted solution consists of three active feet, each composed of a flexible blade and a space qualified position linear actuator (Cedrat APA 50XS), allowing control of the rigid-body motion of the mirror. In this way, the isostatic mount has a negligible impact on the deformation of the mirror and provides the best authority with respect to other mounts (e.g., a clamped design). Figure 2 shows a global view of the AO mirror supported by the isostatic support.

It is worth noting that the piezoelectric actuators work in a nonsymmetric voltage range, $[V_{min}, V_{max}]$ with $V_{min} < 0$, $V_{max} > 0$, and $|V_{min}| \ll V_{max}$ (e.g., for the 200-μm-thick PIC-252 PZT, $V_{min} = -80$ V, and $V_{max} = 400$ V). Since symmetrical positive and negative deformations are required, this would restrict the maximal voltage range to $\Delta V_{max} = 160$ V. To cope with this, the PZT patch is glued under a uniform voltage (using space qualified glue, EPO-TEK-301), according to the technique described in Ref. [15], so that the static shape of the mirror is concave. Therefore, a bias voltage is necessary to make the mirror flat. This allows deformation of the mirror in both directions with only positive voltages while using the full voltage range ($\Delta V_{max} = 480$ V).

The upper diagram of Fig. 3 refers to the wafer as received from Si-Mat, while the lower one corresponds to the situation after gluing the PZT on the wafer and mounting the DM on the isostatic support. The Zernike mode decomposition of the surface figure is shown; the left part of the spectrum shows the surface figure, whereas the right part of the spectrum shows

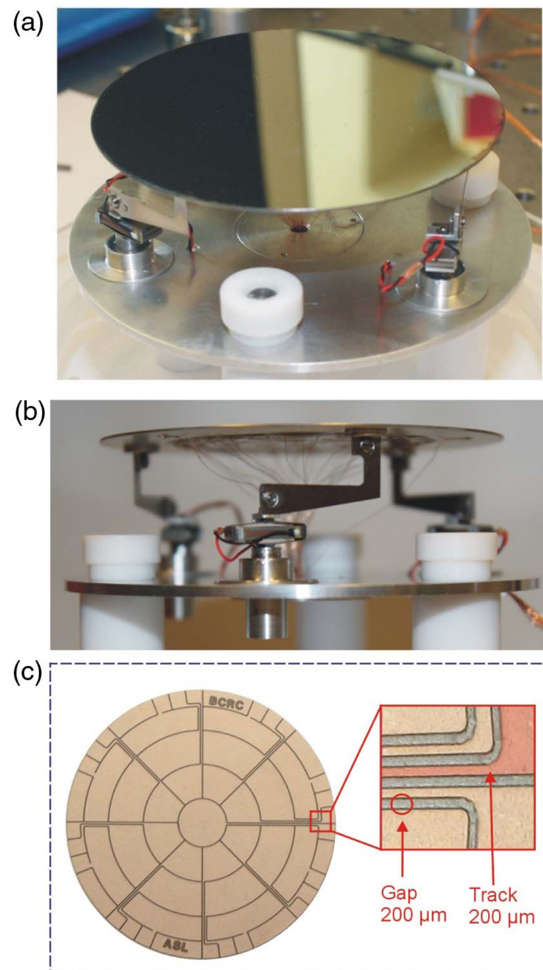

Fig. 2. AO mirror with PZT actuation: (a) front view. (b) Side view with isostatic support and piston-tip–tilt actuators. (c) Electrodes with keystone design and connecting tracks.

the “high-frequency terms”, which is the residual when the first 15 Zernike modes have been removed (those that will be easily cancelled by control). One sees that the PV amplitude increases from 2.8 to 22.6 μm (in a pupil diameter of 34.5 mm) due to the defocus introduced during the gluing under voltage (it will disappear when the bias voltage is applied) and that the high-frequency residual passed from 10 to 37 nm during the gluing process (for unknown reason). Note that if nonuniform voltages are used during the gluing process, it is possible to achieve more elaborate free initial forms [16].

B. Finite Element Model

The whole DM, including the active feet, has been analyzed with the F.E. software SAMCEF. Standard triangular and quadrangular plate/shell elements are used to mesh the DM and the bending blades. Volume elements are used to represent the interface parts (the layer of 3M adhesive tape bonding the wafer on the upper part of the blades). The mesh is chosen with an adequate density to model all the local effects accurately. The mechanical behavior of the mirror is modeled using multilayered Mindlin formulation. The thickness and material properties of each layer are defined independently. The single-crystal

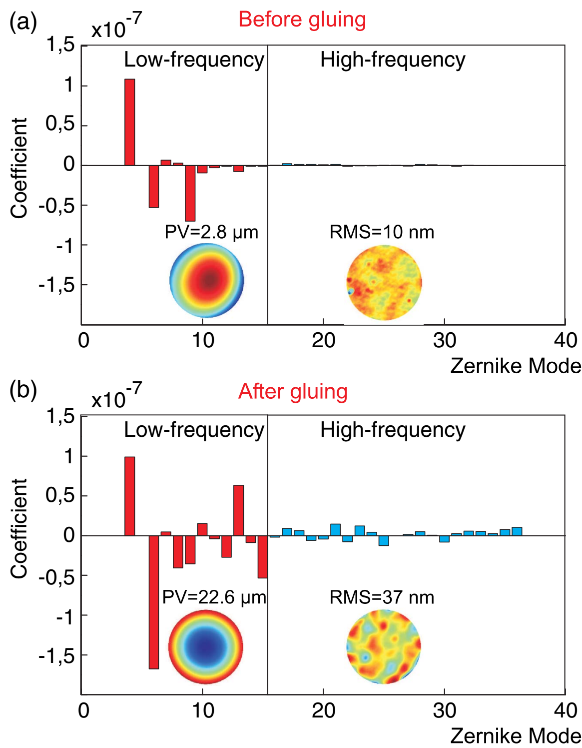

Fig. 3. (a) Mirror shape as received from Si-Mat. (b) Mirror shape after gluing. The left part of the spectrum shows the surface figure, whereas the right part of the spectrum shows the "high-frequency terms" (from Z_{15} to Z_{∞}). A global defocus of 22.6 μm is given to the mirror during the gluing process under bias voltage. Note also that the high-frequency residual has increased during the gluing process. The results are shown in a pupil diameter of 34.5 mm. Note that the defocus coefficient has been removed from the spectrum for clarity (because of the order of magnitude difference).

Si wafer used in this study is cut in the [1,0,0] plane; although weakly orthotropic [17], numerical models with isotropic average properties have been found sufficient for numerical predictions. The PZT actuators are modeled by a layer with the properties of a piezoelectric material. This module was developed at the Active Structures Laboratory [18,19] and subsequently implemented as a standard tool in SAMCEF. The model allows to easily implement combinations of an arbitrary set of layers to represent any design option that may be worth studying. In practice, comparisons between experimental and numerical results have shown that only the layers of Si and PZT have a significant influence; all the other layers can be neglected.

C. Control Algorithm

The surface figure of the mirror $\mathbf{w}$ and the voltages $\mathbf{v}$ applied to the various electrodes are related by the Jacobian (assuming linear piezoelectricity):

$$\mathbf{w} = \mathbf{J}\mathbf{v}. \quad (1)$$

The voltage distribution necessary to achieve a given shape is obtained by inverting this relationship:

$$\mathbf{v} = \mathbf{J}^{\dagger}\mathbf{w}. \quad (2)$$

However, the ill-conditioning of the Jacobian is responsible for large voltage values when the Moore–Penrose inverse $\mathbf{J}^{\dagger} = (\mathbf{J}^T\mathbf{J})^{-1}\mathbf{J}^T$ is used. This problem can be alleviated using one of the following equivalent methods:

1. Using the singular value decomposition of $\mathbf{J}$ and truncating the lowest singular values when computing $\mathbf{J}^{\dagger}$ [20].

2. Using a *Tikhonov regularization*, also known as DLS [21], replacing the Moore–Penrose inverse by $\mathbf{J}^{\dagger} = (\mathbf{J}^T\mathbf{J} + \alpha^2\mathbf{I})^{-1}\mathbf{J}^T$, where α is the damping factor and weighs the conflicting requirements of minimizing the surface figure error at the sensor and minimizing the voltage budget.

The two options are compared in Fig. 4 when the target surface is a coma of 1 μm amplitude: the upper figure shows the singular values σ_i^2 of $\mathbf{J}^T\mathbf{J}$ and those of $(\mathbf{J}^T\mathbf{J} + \alpha^2\mathbf{I})$ for a given value of α. The lower figures show the voltage distribution, respectively, from left to right, when (i) the Moore–Penrose is used [the condition number of $\mathbf{J}$ is $c(\mathbf{J}) = 10^4$], (ii) the three lowest singular values are truncated [reducing to $c(\mathbf{J}) = 10^3$], and (iii) the DLS is used [in such a way that $c(\mathbf{J}^T\mathbf{J} + \alpha^2\mathbf{I}) = 10^6$]. The two methods lead to equivalent results and produce a substantial reduction of the voltage budget (from 211 V to about 50 V) to achieve very similar results. The control algorithm is essentially the same as that used in Ref. [22]. In order to compensate for the hysteresis of the piezoelectric actuators, the algorithm must be applied iteratively until convergence is reached (i.e., in closed-loop, as shown in Fig. 5).

Figure 6 shows the residual static error when the fabricated mirror is corrected to be flat. The central figure shows the experimental results in a pupil of 30 mm. The residual error is

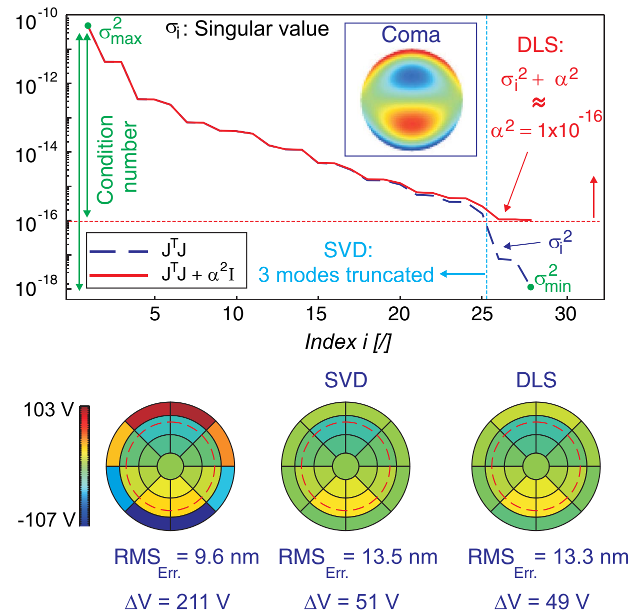

Fig. 4. Top: singular values σ_i^2 of $\mathbf{J}^T\mathbf{J}$ and those of $(\mathbf{J}^T\mathbf{J} + \alpha^2\mathbf{I})$ for some value of α. Bottom: voltage distribution leading to a coma of 1 μm; Left: Moore–Penrose inverse [the condition number of $\mathbf{J}$ is $c(\mathbf{J}) = 10^4$]; center: the lowest three singular values are truncated [reducing to $c(\mathbf{J}) = 10^3$], right: the DLS is used [in such a way that $c(\mathbf{J}^T\mathbf{J} + \alpha^2\mathbf{I}) = 10^6$].

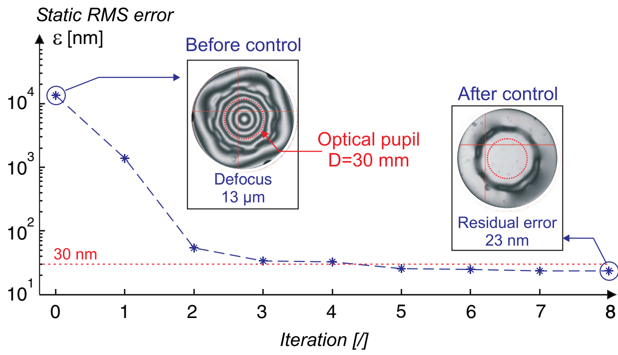

Fig. 5. Experimental results: convergence curve when the DLS algorithm is applied iteratively to achieve a flat configuration. The figure also shows the interferometry fringes measured with a NIMO wavefront sensor.

23.5 nm; it is fully consistent with the numerical F.E. results shown in the left side. The bias voltage is 95 V, and the control voltage around the bias voltage is $\Delta V = 30$ V. The right side of the figure shows the residual figure error when the first 15 Zernike modes are removed from the global surface figure error. One can see that no further reduction of the RMS error is achieved, which indicates that the residual error is orthogonal to the low-order Zernike modes, which are well controlled.

D. Experimental Results

In this section, we discuss the various experiments conducted on the mirror presented in Fig. 2. These experiments are intended to demonstrate the compliance of the proposed DM with the requirements set by ESA.

1. Zernike Modes

Figure 7 presents the ability of the prototype to generate the first 15 Zernike modes. The measurements have been performed using a high-resolution phase-shift Schlieren NIMO RE2507 wavefront sensor from Lambda-X [23]. All the required modes, as well as the optional modes (except the optional vertical Tetrafoil), are fully compliant with the requirements set by ESA in terms of RMS error and voltage range

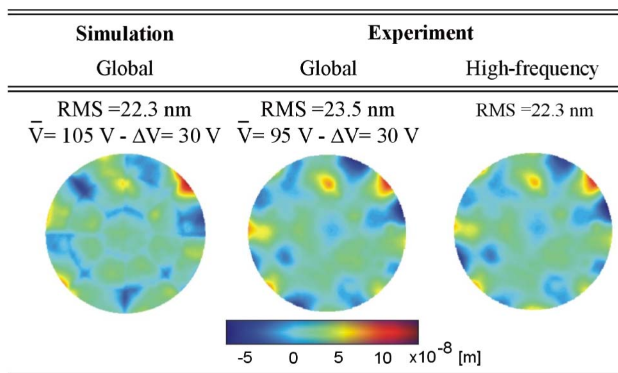

Fig. 6. Residual surface figure error when the fabricated AO mirror is corrected to be flat. Left: numerical F.E. simulation. Center: experiment. Right: high-frequency residual error when 15 Zernike modes have been removed.

ΔV. The voltage range required to generate the amplitude of the desired Zernike modes is much lower than the maximal voltage range that can be applied on the PZT ($\Delta V_{max} = 400$ V for a 200-µm-thick PZT), such that this design allows generation of higher amplitudes than those required by ESA. It is worth noting that the residual static error shown in Fig. 6 affects the total error of the Zernike modes and is constant regardless of the amplitude of the generated shape. The agreement between the numerical simulations and the experimental results is almost perfect when the static error is removed from the measurements (relative measurement). This is shown in Fig. 8, where the target shape is a 1 µm astigmatism, superimposed on the static shape of the mirror. The left side of the figure shows the numerical simulation, while the right side shows the experimental result. The incremental surface figure, the voltage map on the 25 electrodes, and the surface figure error are shown from top to bottom. One can note that: (i) the error pattern, as well as the voltages, are fully consistent with the F.E. model, and (ii) the RMS error is almost two times smaller than the result presented in Fig. 7.

2. Open-Loop Long-Term Stability

The DM has been used for monitoring the creep of its piezoelectric response. For this experiment, it was deliberately chosen not to generate a defocus to discriminate the effect of temperature variations from creep. Therefore, the shape generated was an astigmatism with an amplitude of 2 µm. The creep test consisted of maintaining the voltage pattern for 1 h and monitoring over time the evolution of the resulting shape. The esults are shown in Fig. 9. One can see that without taking into account the defocus component, the RMS error with respect to the 2 µm amplitude astigmatism passed from 20 nm ($t = 0$) to 24 nm (after 1 h). It is also worth noting that if the astigmatism component of the error is removed, the RMS error is constant, which means that the creep is homogeneous for all the actuators, and a small uniform gain on the voltages is sufficient to compensate for the low creep. Observe that all the curves stay within the requirement (RMS error <30 nm over 1 h).

3. Natural Frequencies

Figure 10 shows the result of a modal analysis conducted on the mirror, using the central electrode to excite the mirror and a Polytec scanner vibrometer as sensor. The lowest frequency is at 243 Hz and corresponds to a piston mode, likely to be due to a double sided tape at the connection between the flexible blades and the mirror. Note that the first flexible mode of the mirror is higher than 750 Hz. Figure 11 shows a new ultra-flat design, which has been obtained by changing the position of the piston-tip–tilt actuators; this configuration is more compact and has a first mode at 350 Hz (the double sided tape has been replaced by the space qualified glue, EPO-TEK-301), which is more than two times higher than the requirement (140 Hz).

3. PART 2

While the first part of the paper presents the experimental performance of the DM developed in the framework of the ESA project, the following part presents additional considerations purely based on numerical simulations for a future work.

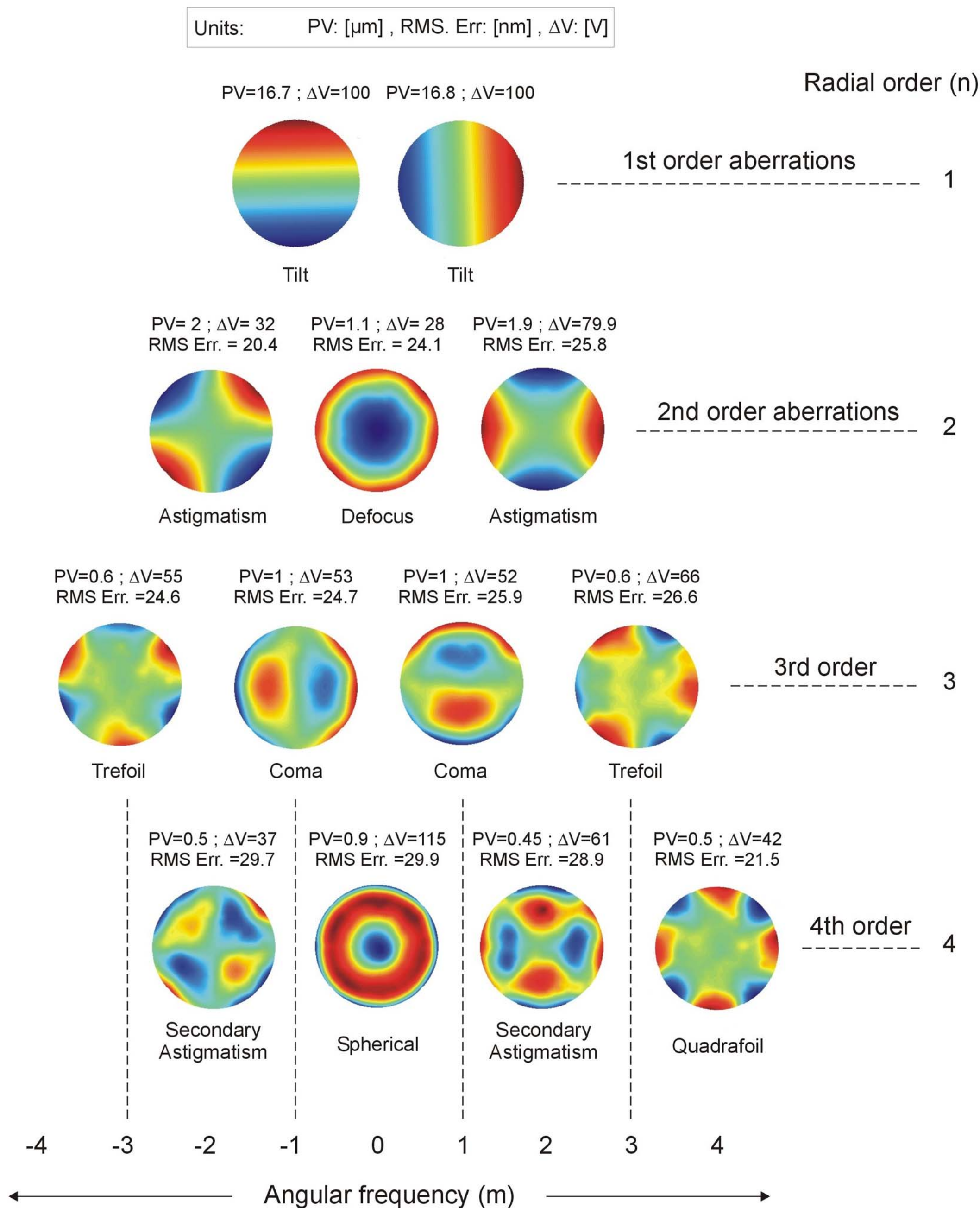

Fig. 7. Experimental performance measured for the first 15 Zernike modes in a pupil of 30 mm. All the required modes, as well as the optional modes, are fully compliant with the requirements set by ESA in terms of RMS error and voltage range (RMS error <30 nm, and $\Delta V < 200$ V). The static error shown in Fig. 6 affects the total error of the Zernike modes. The agreement between the numerical simulations and the experimental results is almost perfect when the static error is removed, as shown in Fig. 8.

A. Thermal Stability: Aluminum Ring

The unimorph architecture is inherently sensitive to temperature variations because of the thermal differential expansion between the PZT and the Si substrate. The ability to actively correct the effect of a temperature change ΔT is measured by the ratio between the maximum piezoelectric strain and the thermal differential expansion:

$$\frac{d_{31}E_{\max}}{\Delta\alpha\Delta T}, \tag{3}$$

where $\Delta\alpha = \alpha_1 - \alpha_2$ is the CTE mismatch between the PZT and the Si, d_{31} is the in-plane piezoelectric coefficient, and $E_{\max}$ is the maximum electric field. $d_{31}E_{\max}/\Delta\alpha$ is the largest temperature difference, which can be corrected by a piezoelectric layer for a given mismatch of CTE. It can also be regarded as a figure of merit of the unimorph mirror. Obviously, the higher the voltage range required to compensate for thermal distortion, the lower the available voltage range to compensate for other kinds of aberrations. It is worth noting that the DM shape can be tailored so as to be flat at a given

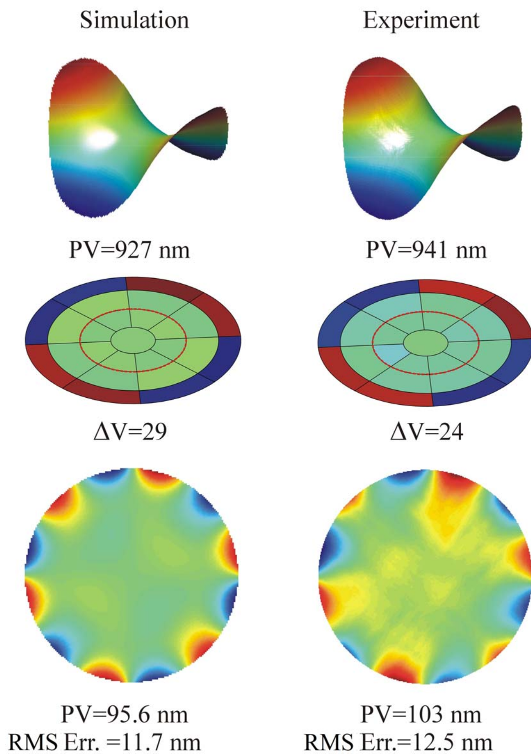

Fig. 8. Comparison of numerical simulation and experiment for an incremental surface of a 1 μm astigmatism. From top to bottom: surface figure, voltage map, and residual error. The result is shown in an optical pupil of 34.5 mm diameter (marked in red on the voltage map).

temperature (one just has to multiply the voltages by a uniform gain during the gluing under voltage process). However, a temperature variation of 20°C around the nominal temperature will induce a 15 μm PV defocus in a pupil diameter of 34.5 mm (for a CTE mismatch $\Delta\alpha = 3.4 \cdot 10^{-6}/\mathrm{K}$). This amplitude requires 20% of the voltage range to be compensated. Table 3

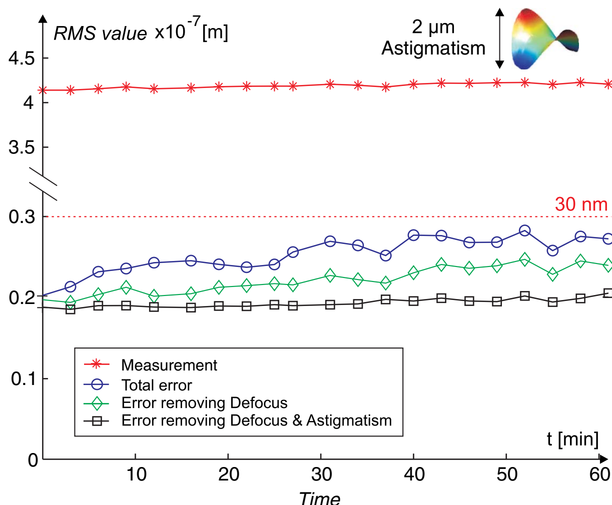

Fig. 9. Creep test during 1 h: evolution of the RMS value of the total shape and of the RMS error.

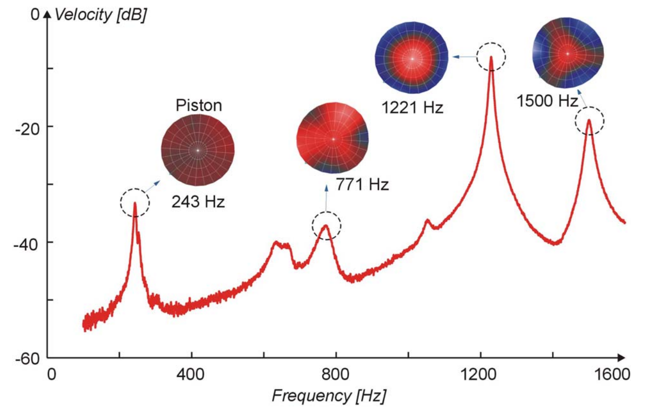

Fig. 10. Average spectrum (magnitude of the velocity) of the frequency response and the corresponding mode shapes of the AO mirror (the excitation is a voltage applied to the central patch).

provides the main thermomechanical properties of the materials used in the unimorph mirror.

A design allowing coping with thermal distortion is presented in Fig. 12. It includes an aluminum ring deposited on the optical face of the DM. This configuration is based on the observation that the differential expansion of the ring with respect to the mirror leads to a uniform curvature in the inner-ring area (in the opposite way as the piezoelectric patch does). Indeed, let us first consider a plate system composed of a stress bearing film of thickness t_f deposited on a substrate of thickness t [Fig. 13(a)].

Let us also assume that the stress in the film is due to a mismatch of CTE:

$$\sigma_f = M_f \Delta\alpha \Delta T, \tag{4}$$

where M_f is the biaxial Young's modulus of the film. The curvature resulting from the stress in a thin film when it covers the full area of the substrate ($R_f = R$) is given by the well-known Stoney's formula [24,25]:

$$\kappa = \frac{6t_f}{Mt^2}\sigma_f, \tag{5}$$

where M is the biaxial Young's modulus of the substrate, $M = Y/(1-\nu)$. This is illustrated in Fig. 14 [Eq. (5)] for an Al film (10 μm thickness) deposited on a Si substrate (500 μm thickness).

Conversely, the curvature resulting from a stress bearing film, whose radius is smaller than the substrate radius ($R_f < R$), is given by [26]

$$\kappa_p = \frac{6t_f}{Mt^2}\left[1 - \frac{1-\nu}{2}\left(1 - \frac{R_f^2}{R^2}\right)\right]\sigma_f \qquad (r \le R_f), \tag{6}$$

where ν is the Poisson's ratio of the substrate. The curvature state is constant and isotropic within $r \le R_f$. For film and substrate of same radius, the above relation degenerates Stoney's formula.

Finally, the curvature κ_r in the inner-ring area, induced by a stress bearing ring-shape film of thickness t_f, is deduced by subtracting Eq. (6) from Eq. (5). In other words,

$$\kappa_r + \kappa_p = \kappa. \tag{7}$$

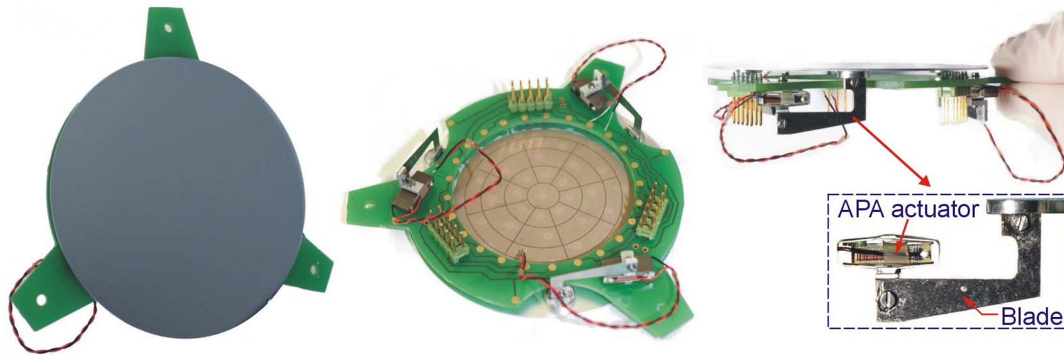

Fig. 11. New light and ultra-flat design with a first mode at 350 Hz.

Table 3. Main Thermomechanical Properties of the Materials Used in the Unimorph Mirror

	Si	PZT	Al
Young's modulus Y [GPa]	130	62	69
Poisson's ratio ν	0.28	0.34	0.33
Density ϱ [kg/m^3]	2330	7800	2700
Y/ϱ [MNm/kg]	56	7	—
CTE α [10^{-6}/K]	2.6	4–8	23
Micro-roughness [nm]	0.1	—	—
E_{max} [V/μm]	—	2	—
d_{31} [10^{-12} m/V]	—	−180	—

Therefore,

$$\kappa_r = \frac{6t_f}{Mt^2}\left[\frac{1-\nu}{2}\left(1-\frac{R_f^2}{R^2}\right)\right]\sigma_f \qquad (r \le R_f). \tag{8}$$

Since the curvature given by Stoney's formula and that given by Eq. (6) are constant and isotropic, the curvature given by

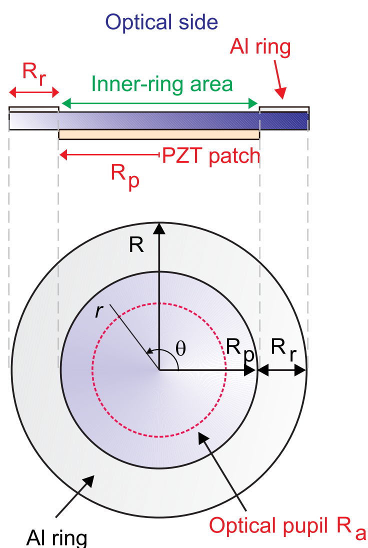

Fig. 12. Top: schematic view of the DM cross-section. Bottom: optical face of the mirror with an Al ring outside the patch area. The inner-ring area is defined for $r < R_p$, where the polar coordinates are used (r, θ).

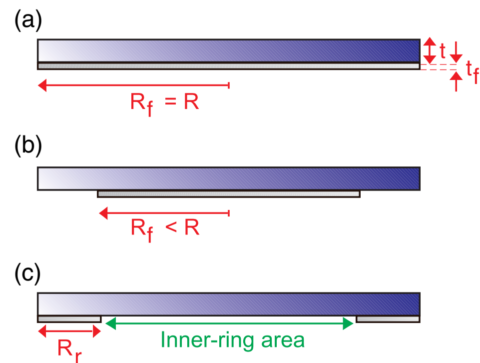

Fig. 13. (a) Thin film covers the whole area of the substrate. (b) The radius of the thin film is smaller than that of the substrate. (c) Ring-shape thin film.

Eq. (8) is also uniform in the inner-ring area, as shown in Fig. 14. This behavior is confirmed by the F.E. computations.

Equation (8) shows that the curvature of the mirror in the inner-ring area does depend linearly on the thickness of the ring. Since the total curvature in the inner-ring area κ is the sum of the curvature induced by the patch κ_p and that induced by the ring κ_r, it is always possible to find a ring thickness t_r, which rigorously compensates the curvature induced by the CTE mismatch between the PZT and the Si. This is illustrated in Fig. 15.

B. Thermal Stability and Control: PZT Ring

The previous section shows that an Al ring deposited on the optical face of the mirror allows counteraction of the distortion of the mirror induced by the CTE mismatch of its layers. However, this relies on the hypothesis that the CTE ratio of the patch and of the ring does not vary too much with the temperature. Conversely, if both the central patch and the ring are made of PZT, the mirror can be made thermally balanced regardless of the temperature range. Furthermore, one can take advantage of the PZT ring to drive the mirror with only positive voltages (the ring allows production of a concave deformation, whereas the central patch is used to deform the mirror in a convex way). Indeed, the stress induced in the mirror by a piezoelectric layer is written as

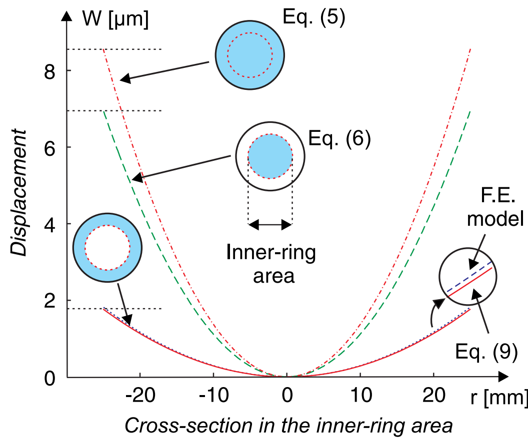

Fig. 14. Curvature induced by a film covering the whole area of the mirror is the sum of the curvature induced by the patch and that induced by the ring. The curvature deduced from Eq. (8) is in very good agreement with the F.E. model for thin films (in this case $\Delta T = 10°\mathrm{K}$). The thicknesses of the Al layer and the Si substrate are, respectively, 10 and 500 μm; the radii of the mirror and the central part are, respectively, $R = 38.1$ mm, and $R_p = 25$ mm.

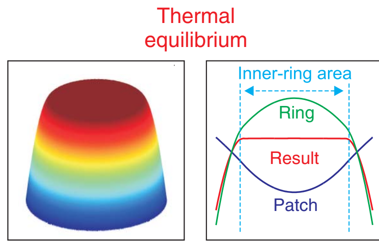

Fig. 15. Numerical simulation of an Al ring compensating the thermal distortion in the inner-ring area. The substrate is a 500 μm Si wafer with a diameter of 76.2 mm, the PZT has a thickness of 200 μm, and a diameter of 50 mm; the Al ring has a thickness of 50 μm.

$$\sigma_f = M_f d_{31} E, \tag{9}$$

where E is the electric field in the PZT. Equations (4) and (9) show the analogy between the piezoelectric and thermal effects. Therefore, the steps to control the mirror are as follows:

1. Apply a voltage on the ring to achieve a concave curvature.

2. Maintain the voltage on the ring and apply a voltage on the patch to compensate for the concave curvature. The mirror is now flat in the inner-ring area.

3. The mirror can be used in both directions only by changing the voltage on the central patch.

As an example, Fig. 16 illustrates the particular case where the thickness of the ring is chosen such that the deformation range for the control is symmetric. To do so, the maximal deformation achievable with the central patch has to be twice that of the ring. By analogy between the piezoelectric and thermal

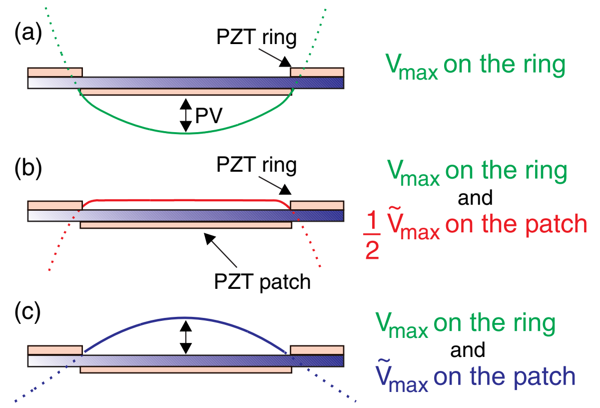

Fig. 16. $V_{\max}$ and $\tilde{V}_{\max}$ are, respectively, the maximum voltage that can be applied on the patch and on the ring. In this example, the ring is 1.5 times thicker than the patch, hence, $V_{\max} = 1.5\tilde{V}_{\max}$. This leads to a symmetric deformation range [the PV of case (a) is equal to that of case (c)].

effect, it follows that under these conditions the PZT ring makes the mirror two times less sensitive to thermal distortion. More generally, the thickness of the ring can be chosen so as to achieve a perfectly thermally balanced design [27].

4. CONCLUSION

The first part of the paper presents the performance of an AO mirror intended to be used as a secondary corrector in space telescopes. The manufactured DM was tested in terms of RMS wavefront error (smaller than 30 nm for the first 15 Zernike modes), open-loop long-term stability, voltage budget (only positive voltages are used), rigid-body actuation, reflectivity, and lowest eigen frequency. It turned out that the unimorph AO mirror is fully compliant with the goals set by ESA, corresponding to a technology readiness level of 4 (TRL 4). A new design has been obtained by changing the position of the piston-tip–tilt actuators, leading to a more compact and ultra-light configuration with a first mode at 350 Hz. The demonstrator uses only space qualified components, but environmental tests remain to be completed to reach TRL 5.

The second part of the paper demonstrates analytically and numerically that an Al ring deposited on the optical face of the mirror can be used to achieve a thermally balanced design. By analogy between the thermal and piezoelectric effects, it is then showed that a PZT ring on the optical face of the mirror can be combined with the central PZT patch to drive the mirror in both directions with only positive voltages, while reducing its sensitivity to temperature variations. It is worthwhile to point out that this concept is very robust from a thermal point of view, since the ring and the central patch are made of the same material, and no initial static curvature is needed on the mirror. Furthermore, there is no risk to damage the piezoelectric patches, since the mirror is driven with only positive voltages.

Funding. European Space Agency (ESA); Fonds De La Recherche Scientifique - FNRS (FNRS).

Acknowledgment. This study was supported by the European Space Agency (ESA) within the GSTP program BIALOM: Bimorph Adaptive Large Optical Mirror Demonstrator, with Eric Wille as the technical officer. The authors also gratefully acknowledge AMOS and the Centre Spatial de Lige (CSL), the industrial partners of the consortium. R. Bastaits was supported by FNRS, K. Wang by the China Scholarship Council, and B. Mokrani by the Walloon Region.

REFERENCES

1. J. W. Hardy, *Adaptive Optics for Astronomical Telescopes* (Oxford University, 1998).
2. P.-Y. Madec, "Overview of deformable mirror technologies for adaptive optics and astronomy," Proc. SPIE **8447**, 844705 (2012).
3. I. Bekey, *Advanced Space System Concepts and Technologies, 2010-2030+* (AIAA, 2003).
4. C. H. M. Jenkins, ed., *Gossamer Spacecraft: Membrane and Inflatable Structures Technology for Space Applications*, Progress in Astronautics and Aeronautics (AIAA, 2001), Vol. 191.
5. K. Patterson and S. Pellegrino, "Ultralightweight deformable mirrors," Appl. Opt. **52**, 5327–5341 (2013).
6. P. Rausch, S. Verpoort, and U. Wittrock, "Unimorph deformable mirror for space telescopes: design and manufacturing," Opt. Express **23**, 19469–19477 (2015).
7. P. Rausch, S. Verpoort, and U. Wittrock, "Unimorph deformable mirror for space telescopes: environmental testing," Opt. Express **24**, 1528–1542 (2016).
8. W. G. Cady, *Piezoelectricity* (McGraw-Hill, 1946).
9. ESA, "Bimorph adaptive large optical mirror demonstrator," ESA/ESTEC contract NO. 400010294/11/NL/CP.
10. J. Ma, Y. Liu, T. He, B. Li, and J. Chu, "Double drive modes unimorph deformable mirror for low-cost adaptive optics," Appl. Opt. **50**, 5647–5654 (2011).
11. H. Park and D. A. Horsley, "Single-crystal PMN-PT MEMS deformable mirrors," J. Microelectromech. Syst. **20**, 1473–1482 (2011).
12. N. T. Adelman, "Spherical mirror with piezoelectrically controlled curvature," Appl. Opt. **16**, 3075–3076 (1977).
13. S. A. Kokorowski, "Analysis of adaptive optical elements made from piezoelectric bimorphs," J. Opt. Soc. Am. **69**, 181–187 (1979).
14. E. Steinhaus and S. Lipson, "Bimorph piezoelectric flexible mirror," J. Opt. Soc. Am. **69**, 478–481 (1979).
15. R. Bastaits, D. Alaluf, M. Horodinca, I. Romanescu, I. Burda, G. Martic, G. Rodrigues, and A. Preumont, "Segmented bimorph mirrors for adaptive optics: segment design and experiment," Appl. Opt. **53**, 6635–6642 (2014).
16. A. Preumont, R. Bastaits, D. Alaluf, M. Horodinca, I. Romanescu, and I. Burda, "The shaping of free form mirrors without polishing," in *ACTUATOR*, Bremen, Germany, June 2014.
17. M. A. Hopcroft, W. D. Nix, and T. W. Kenny, "What is the Young's modulus of silicon?" J. Microelectromech. Syst. **19**, 229–238 (2010).
18. V. Piefort, N. Loix, and A. Preumont, "Modeling of piezolaminated composite shells for vibration control," in *ESA Conference on Spacecraft Structures, Materials and Mechanical Testing*, Braunschweig, Germany, November 1998 (ESA SP-428, 1999).
19. V. Piefort, "Finite element modeling of piezoelectric active structures," Ph.D. thesis (Université Libre de Bruxelles, Active Structures Laboratory, 2001).
20. A. M. Maciejewski and C. A. Klein, "The singular value decomposition: computation and applications to robotics," Int. J. Robot. Res. **8**, 63–79 (1989).
21. C. W. Wampler, "Manipulator inverse kinematic solutions based on vector formulations and damped least-squares methods," IEEE Trans. Syst. Man Cybern. **16**, 93–101 (1986).
22. R. Bastaits, D. Alaluf, E. Belloni, G. Rodrigues, and A. Preumont, "Segmented bimorph mirrors for adaptive optics: morphing strategy," Appl. Opt. **53**, 4825–4832 (2014).
23. L. Joannes, F. Dubois, and J.-C. Legros, "Phase-shifting schlieren: high-resolution quantitative schlieren that uses the phase-shifting technique principle," Appl. Opt. **42**, 5046–5053 (2003).
24. B. Bhushan, ed., "Thermomechanics of multilayer thin-film microstructures," in *Springer Handbook of Nanotechnology* (Springer, 2004), Part E, Chap. 35.1.
25. L. B. Freund and S. Suresh, *Thin Film Materials, Stress, Defect Formation and Surface Evolution* (Cambridge University, 2003).
26. X. Feng, Y. Huang, H. Jiang, D. Ngo, and A. J. Rosakis, "The effect of thin film/substrate radii on the Stoney formula for thin film/substrate subjected to nonuniform axisymmetric misfit strain and temperature," J. Mech. Mater. Struct. **1**, 1041–1053 (2006).
27. D. Alaluf, "Piezoelectric mirrors for adaptive optics in space telescopes," Ph.D. thesis (Université Libre de Bruxelles, Active Structures Laboratory, 2016).

131.176.243.12 {ts '2018-05-02 04:03:59'}